

# Optimization of thermal ghost imaging: high-order correlations vs. background subtraction

Kam Wai C. Chan,\* Malcolm N. O'Sullivan, and Robert W. Boyd

*The Institute of Optics, University of Rochester, Rochester, New York 14627, USA*

*\* Present address: Rochester Optical Manufacturing Company, 1260 Lyell Avenue, Rochester, New York 14606, USA*

[kwchan@optics.rochester.edu](mailto:kwchan@optics.rochester.edu)

**Abstract:** We compare the performance of high-order thermal ghost imaging with that of conventional (that is, lowest-order) thermal ghost imaging for different data processing methods. Particular attention is given to high-order thermal ghost imaging with background normalization and conventional ghost imaging with background subtraction. The contrast-to-noise ratio (CNR) of the ghost image is used as the figure of merit for the comparison. We find analytically that the CNR of the normalized high-order ghost image is inversely proportional to the square root of the number of transmitting pixels of the object. This scaling law is independent of the exponents used in calculating the high-order correlation and is the same as that of conventional ghost imaging with background subtraction. We find that no data processing procedure performs better than lowest-order ghost imaging with background subtraction. Our results are found to be able to explain the observations of a recent experiment [Chen et al., arXiv:0902.3713v3 [quant-ph]].

© 2010 Optical Society of America

**OCIS codes:** (110.1650) Coherence imaging; (030.4280) Noise in imaging systems

---

## References and links

1. T. B. Pittman, Y. H. Shih, D. V. Strekalov, and A. V. Sergienko, "Optical imaging by means of two-photon quantum entanglement," *Phys. Rev. A* **52**, R3429–R3432 (1995).
2. A. Gatti, E. Brambilla, M. Bache, and L. A. Lugiato, "Ghost Imaging with Thermal Light: Comparing Entanglement and Classical Correlation," *Phys. Rev. Lett.* **93**, 093602 (2004);
3. A. Gatti, E. Brambilla, M. Bache, and L. A. Lugiato, "Correlated imaging, quantum and classical," *Phys. Rev. A* **70**, 013802 (2004).
4. A. Valencia, G. Scarcelli, M. D'Angelo, and Y. H. Shih, "Two-Photon Imaging with Thermal Light," *Phys. Rev. Lett.* **94**, 063601 (2005).
5. Y. Bromberg, O. Katz, and Y. Silberberg, "Ghost imaging with a single detector," *Phys. Rev. A* **79**, 053840 (2009).
6. G. Scarcelli, V. Berardi, and Y. Shih "Can Two-Photon Correlation of Chaotic Light Be Considered as Correlation of Intensity Fluctuations?" *Phys. Rev. Lett.* **96**, 063602 (2006).
7. A. Gatti, M. Bondani, L. A. Lugiato, M. G. A. Paris, and C. Fabre, "Comment on Can Two-Photon Correlation of Chaotic Light Be Considered as Correlation of Intensity Fluctuations?" *Phys. Rev. Lett.* **98**, 039301 (2007).
8. B. I. Erkmen and J. H. Shapiro, "Unified theory of ghost imaging with Gaussian-state light," *Phys. Rev. A* **77**, 043809 (2008).
9. L.-G. Wang, S. Qamar, S.-Y. Zhu, and M. S. Zubairy, "Hanbury Brown-Twiss effect and thermal light ghost imaging: A unified approach," *Phys. Rev. A* **79**, 033835 (2009).
10. J. H. Shapiro, "Computational ghost imaging," *Phys. Rev. A* **78**, 061802 (2008).

11. R. Meyers, K. S. Deacon, and Y. H. Shih, "Ghost-imaging experiment by measuring reflected photons," *Phys. Rev. A* **77**, 041801(R) (2008).
12. J. Cheng and S. Han, "Incoherent Coincidence Imaging and Its Applicability in X-ray Diffraction," *Phys. Rev. Lett.* **92**, 093903 (2004).
13. G. Scarcelli, V. Berardi, and Y. Shih, "Phase-conjugate mirror via two-photon thermal light imaging," *Appl. Phys. Lett.* **88**, 061106 (2006).
14. L. Basano and P. Ottonello, "Experiment in lensless ghost imaging with thermal light," *Appl. Phys. Lett.* **89**, 091109 (2006).
15. F. Ferri, D. Magatti, A. Gatti, M. Bache, E. Brambilla, and L. A. Lugiato, "High-Resolution Ghost Image and Ghost Diffraction Experiments with Thermal Light," *Phys. Rev. Lett.* **94**, 183602 (2005).
16. L. Basano and P. Ottonello, "Use of an intensity threshold to improve the visibility of ghost images produced by incoherent light," *Appl. Opt.* **46**, 6291–6296 (2007).
17. Y. Bai and S. Han, "Ghost imaging with thermal light by third-order correlation," *Phys. Rev. A* **76**, 043828 (2007).
18. L.-H. Ou and L.-M. Kuang, "Ghost imaging with third-order correlated thermal light," *J. Phys. B: At. Mol. Opt. Phys.* **40**, 1833–1844 (2007).
19. D.-Z. Cao, J. Xiong, S.-H. Zhang, L.-F. Lin, L. Gao, and K. Wang, "Enhancing visibility and resolution in Nth-order intensity correlation of thermal light," *Appl. Phys. Lett.* **92**, 201102 (2008).
20. I. N. Agafonov, M. V. Chekhova, T. Sh. Iskhakov, and A. N. Penin, "High-visibility multiphoton interference of Hanbury Brown-Twiss type for classical light," *Phys. Rev. A* **77**, 053801 (2008).
21. Q. Liu, X.-H. Chen, K.-H. Luo, W. Wu, and L.-A. Wu, "Role of multiphoton bunching in high-order ghost imaging with thermal light sources," *Phys. Rev. A* **79**, 053844 (2009).
22. K. W. C. Chan, M. N. O'Sullivan, and R. W. Boyd, "High-Order Thermal Ghost Imaging," *Opt. Lett.* **34**, 3343–3345 (2009).
23. X.-H. Chen, I. N. Agafonov, K.-H. Luo, Q. Liu, R. Xian, M. V. Chekhova, L.-A. Wu, "Arbitrary-order lensless ghost imaging with thermal light," arXiv:0902.3713v3 [quant-ph].
24. O. Katz, Y. Bromberg, and Y. Silberberg, "Compressive ghost imaging," *Appl. Phys. Lett.* **95**, 131110 (2009).
25. L. Basano and P. Ottonello, "A conceptual experiment on single-beam coincidence detection with pseudothermal light," *Opt. Express* **15**, 12386–12394 (2007).
26. D. Cao, J. Xiong, and K. Wang, "Geometrical optics in correlated imaging systems," *Phys. Rev. A* **71**, 013801 (2005).
27. Y. Cai and F. Wang, "Lensless imaging with partially coherent light," *Opt. Lett.* **32**, 205–207 (2007).
28. B. I. Erkmen and J. H. Shapiro, "Signal-to-noise ratio of Gaussian-state ghost imaging," *Phys. Rev. A* **79**, 023833 (2009).
29. D. Zhang, Y.-H. Zhai, L.-A. Wu, and X.-H. Chen, "Correlated two-photon imaging with true thermal light," *Opt. Lett.* **30**, 2354–2356 (2005).
30. D. V. Hinkley, "On the Ratio of Two Correlated Normal Random Variables," *Biometrika* **56**, 635–639 (1969).
31. A. Cedilnik, K. Košmelj, and A. Blejec, "Ratio of Two Random Variables: A Note on the Existence of its Moments," *Metodološki zvezki* **3**, 1–7 (2006).
32. R. C. Geary, "The Frequency Distribution of the Quotient of Two Normal Variates," *J. Roy. Statistical Society* **93**, 442–446 (1930).
33. K. N. Boyadzhiev, "Exponential Polynomials, Stirling Numbers, and Evaluation of Some Gamma Integrals," *Abstract and Applied Analysis* **2009**, 168672 (2009).
34. S. Roman, *The Umbral Calculus* (Academic Press, New York, 1984), pp. 63–67 and 82–87.

## 1. Introduction

Ghost imaging is a novel imaging technique that acquires the image of an object with the processes of object interrogation and image formation performed separately [1, 2, 3, 4]. In a typical ghost imaging setup, two mutually correlated beams of light are used: an object field that illuminates the object but is not spatially resolved by its detector and a reference field that does not interact with the object but is spatially resolved by its detector. The ghost image is then obtained by measuring the intensity cross-correlation function of the object and reference fields.

There are two main categories of light sources used for ghost imaging: entangled photons produced in parametric down-conversion [1] and spatially incoherent pseudo-thermal light produced by a laser beam with a rotating diffuser [4] or a spatial light modulator [5]. The setup that uses pseudo-thermal light has attracted a lot of attention recently due to its potential practical applications as well as the interpretation of its underlying physical process [6, 7, 8, 9, 10, 11].

While there are similarities and differences in the ghost images produced by the two different light sources, the most notable difference between the two is that a thermal ghost image always lies on a noisy background whereas the ghost image obtained using entangled photons can achieve 100% visibility.

The conventional method to improve the contrast of a thermal ghost image is by simple background subtraction [2, 3, 6, 11, 12, 13, 14, 15]. Another means of increasing the visibility of the ghost image is by selecting workable reference speckle patterns using a threshold level [16]. More recently, high-order intensity correlations have been utilized for the same goal [17, 18, 19, 20, 21, 22, 23]. In addition, ghost image reconstruction based on compressive sampling to achieve high sampling efficiency and good image quality has been demonstrated [24]. It should be noted that different methods of data processing of the object and reference signals lead to ghost images with different qualities. For example, high-order ghost imaging without normalization by the background intensity is found theoretically to attain an optimal image quality at a power order of the correlation that depends on the transmitting area of the object [22], whereas no such optimal behavior is seen in the normalized high-order ghost image in experiment [23]. The intent of the present paper is to compare theoretically the performances of different schemes for reconstructing thermal ghost images. Particular attention is given to the important special cases of conventional thermal ghost imaging with background subtraction and high-order thermal ghost imaging with background normalization. We will use the contrast-to-noise ratio (CNR), which is defined in the next section, as the figure of merit for the comparison. Only those methods that are based on the cross-correlation of the object and reference signals are considered in the current work.

In the following, we first calculate the CNR of the conventional thermal ghost imaging. The image quality of the high-order thermal ghost imaging is then studied in detail in Section 3. Throughout this paper, the analyses of the ghost image quality are made using classical arguments [22, 25]. We will consider the effects of shot noise using a semi-classical approach in Section 4. The results are summarized in Section 5.

## 2. Conventional thermal ghost imaging

A typical thermal ghost imaging setup is shown in Fig. 1(a). Here we consider the lensless ghost imaging configuration [6, 12, 13, 14, 26, 27]. The spatial patterns of the light beams are generated by a rotating ground glass plate to mimic a thermal light source. To simplify the analysis, the object is taken to be a binary object, i.e., the object mask has either zero or unity transmission. The average size of the speckles is taken to be approximately the same as the size of the pixels of the reference detector. As a result, we can perform a spatial discretization of the intensity of light falling onto the object surface, and the light falling onto a given pixel can be assumed to be statistically independent of that falling onto other pixels (see Fig. 1(b)).

We assume that the photodetector response time is short compared to the correlation time of the speckle field, as is the case in many typical situations. In addition, we assume that the illuminating beam has an essentially uniform intensity distribution over the transverse extent of the object. Specifically, the average intensity of the light beam is taken to have a negative exponential probability distribution of mean  $\langle I(\vec{x}) \rangle \equiv \mu$  for all the positions  $\vec{x}$ , where  $I(\vec{x})$  is the speckle intensity in the object plane and  $\langle \dots \rangle$  denotes ensemble average. We assume that the light source is sufficiently intense that shot noise in the photocurrent leaving each detector element is negligibly small. In Section 4 we examine the conditions under which this assumption is valid. Together with the assumption on the size of the speckles made above, we can conclude that  $\langle I^n(\vec{x}) \rangle = n! \langle I(\vec{x}) \rangle^n = n! \mu^n$  and  $\langle I(\vec{x}) I(\vec{x}') \rangle = \langle I(\vec{x}) \rangle \langle I(\vec{x}') \rangle = \mu^2$  for  $\vec{x} \neq \vec{x}'$ .

The conventional thermal ghost image is obtained by calculating the cross-correlation of the

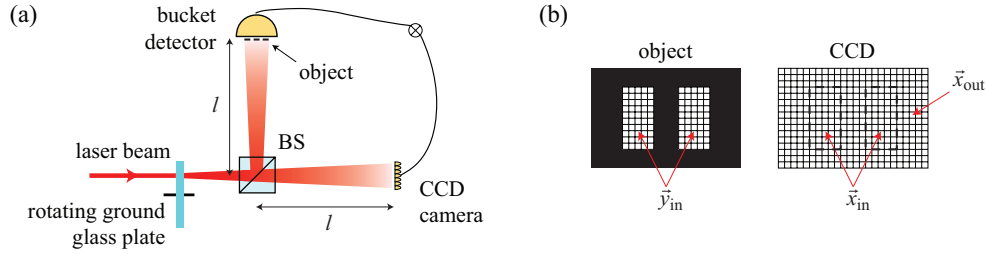


Fig. 1. (a) Schematic of the lenless thermal ghost imaging setup. (b) The simplified object model for analysis. The object plane (left) and the reference detector plane (right) are discretized by pixels of finite sizes. BS: beam-splitter.

object signal  $I_o$  and the reference signal  $I_r(\vec{x})$ :

$$G(\vec{x}) = M[I_o I_r(\vec{x})], \quad (1)$$

where

$$M[X] \equiv \frac{1}{N} \sum_{s=1}^N X^{(s)} \quad (2)$$

is defined to be the sample average of the quantity  $X$  for the  $N$  measurements  $\{X^{(s)}\}$ ,  $s = 1, \dots, N$ . Here

$$I_o = \frac{1}{\Delta} \int_{\text{beam area}} d^2y O(\vec{y}) I(\vec{y}) \rightarrow \sum_{\vec{y} \in \mathcal{T}} I(\vec{y}) \quad (3)$$

and

$$I_r(\vec{x}) = \frac{1}{\Delta} \int_{\text{area of pixel at } \vec{x}} d^2y I(\vec{y}) \rightarrow I(\vec{x}) \quad (4)$$

are the object and reference signals respectively, and  $\Delta$  is the area of a pixel. The pixel index  $\vec{y}$  in Eq. (3) is summed over the transmitting regions  $\mathcal{T}$  of the binary object mask  $O(\vec{y})$ , with the number of transmitting pixels denoted by  $T$  according to the assumption made previously. In the general situation in which the speckle size can be larger than the size of a pixel of the reference detector,  $T$  is given by  $T = (\text{transmitting area of object}) / (\text{average speckle size})$ .

We define the contrast-to-noise ratio (CNR) to be

$$\text{CNR}(G) \equiv \frac{\langle G(\vec{x}_{\text{in}}) \rangle - \langle G(\vec{x}_{\text{out}}) \rangle}{\sqrt{\frac{1}{2} [\Delta^2 G(\vec{x}_{\text{in}}) + \Delta^2 G(\vec{x}_{\text{out}})]}}, \quad (5)$$

where  $\Delta^2 G(\vec{x}) \equiv \langle G(\vec{x})^2 \rangle - \langle G(\vec{x}) \rangle^2$ . Here  $\vec{x}_{\text{in}}$  and  $\vec{x}_{\text{out}}$  represent the pixel positions inside and outside the transmitting regions of the object. The variances  $\Delta^2 G(\vec{x}_{\text{in}})$  and  $\Delta^2 G(\vec{x}_{\text{out}})$  are generally not the same. It follows from Eq. (1) that  $\langle G(\vec{x}) \rangle = \langle I_o I_r(\vec{x}) \rangle$  and

$$\Delta^2 G(\vec{x}) = \frac{1}{N} [\langle I_o^2 I_r^2(\vec{x}) \rangle - \langle I_o I_r(\vec{x}) \rangle^2]. \quad (6)$$

Using the result [22]

$$\langle I_o^m I_r^n(\vec{x}) \rangle = \begin{cases} \frac{\Gamma(T+m+n)n!}{\Gamma(T+n)} \mu^{m+n}, & \text{for } \vec{x} = \vec{x}_{\text{in}}, \\ \frac{\Gamma(T+m)n!}{\Gamma(T)} \mu^{m+n}, & \text{for } \vec{x} = \vec{x}_{\text{out}}, \end{cases} \quad (7)$$

where  $\Gamma(\vec{x})$  is the gamma function, the CNR of  $G(\vec{x})$  is found to be [22, 25]

$$\text{CNR}(G) = \sqrt{\frac{N}{T^2 + 5T + 11/2}}. \quad (8)$$

Note that the numerical coefficients of  $T$  in the denominator of Eq. (8) depend on the specifics of the model used for the correlations of the speckle intensities. Of more general applicability is the scaling law  $\text{CNR}(G) \propto \sqrt{N}/T$  for  $T \gg 1$  that characterizes the quality of the ghost image for this data processing method.

An alternative approach for forming the ghost image is to calculate the correlation of the background-subtracted object and reference signals [2, 3, 6, 11, 12, 13, 14, 15]. Specifically, one calculates the ghost image as

$$\begin{aligned} G'(\vec{x}) &= M[(I_o - M[I_o])(I_r(\vec{x}) - M[I_r(\vec{x})])] \\ &= M[I_o I_r(\vec{x})] - M[I_o]M[I_r(\vec{x})]. \end{aligned} \quad (9)$$

It follows from Eq. (7) that the contrast-to-noise ratio of this method is given by

$$\text{CNR}(G') = \sqrt{\frac{N-1}{T + 7/2 - 3/N}}. \quad (10)$$

The scaling law of this procedure is thus given by  $\text{CNR}(G') \propto \sqrt{N}/T$  [28]. We thus see that  $G'(\vec{x})$  performs much better than  $G(\vec{x})$  for the relevant limit  $T \gg 1$ .

Still another procedure for determining the ghost image is to calculate the normalized correlation function [29]

$$g'_{1,1}(\vec{x}) = \frac{M[I_o I_r(\vec{x})]}{M[I_o]M[I_r(\vec{x})]}. \quad (11)$$

By dividing the correlation function by  $M[I_r(\vec{x})]$ , artifacts associated with the nonuniform response of the CCD detector are largely removed from the final ghost image. We will show below in Section 3 that

$$\text{CNR}(g'_{1,1}) \approx \sqrt{\frac{N}{2T+3}}. \quad (12)$$

Thus  $g'_{1,1}(\vec{x})$  performs approximately as well as  $G'(\vec{x})$ .

It is remarked that at times certain workers have advocated taking the background term  $M[I_o]M[I_r(\vec{x})]$  in Eq. (9) as a constant in the limit of large  $N$ , that is, taking  $M[I_o] \rightarrow \langle I_o \rangle$  and  $M[I_r(\vec{x})] \rightarrow \langle I_r(\vec{x}) \rangle$ . Such a procedure leads to the prediction that the contrast-to-noise ratio scales as

$$\text{CNR}(G') \rightarrow \sqrt{\frac{N}{T + 7/2}}. \quad (13)$$

However, we note that this procedure is somewhat unphysical, as there is no operational way to determine an ensemble average without performing an infinite number of measurements.

### 3. High-order thermal ghost imaging

The procedure of high-order ghost image entails calculating the correlation of powers of the signal and reference intensities rather than the the correlation of the intensities themselves. Different configurations for performing high-order thermal ghost imaging have been described [17, 18, 19, 20, 21, 22, 23]. The simplest procedure is to use the same setup as in

Fig. 1(a), where there is only a single reference detector, and to calculate the normalized high-order intensity correlation [19, 20, 23]

$$g_{mn}^{(\text{full})}(\vec{x}) = \frac{M[I_o^m I_r^n(\vec{x})]}{M[I_o^m] M[I_r^n(\vec{x})]}. \quad (14)$$

Note that the exponents  $m$  and  $n$  in the denominator are inside the averages, so that  $g_{mn}^{(\text{full})}(\vec{x})$  is unity when  $I_o$  and  $I_r(\vec{x})$  are uncorrelated. As mentioned in the last section, the normalization over  $M[I_r^n(\vec{x})]$  also has the advantage of eliminating artifacts in the reference detector that appear as a multiplicative function of  $\vec{x}$  on the reference signal.

Unlike as in the case of Eq. (9), the use of sample averages in Eq. (14) imposes difficulties on the analysis of the properties of the ghost image, as the quantities  $M[I_o^m I_r^n(\vec{x})]$ ,  $M[I_o^m]$  and  $M[I_r^n(\vec{x})]$  are also random variables when the number of measurements  $N$  is finite. It might be tempting to treat the denominator as a constant to simplify the analysis. However, this assumption is inappropriate to describe the noise properties of the normalized ghost image, as we demonstrate below.

To simplify the subsequent analysis, we note that  $M[I_o^m]^{-1}$  is a multiplicative factor that is independent of the position  $\vec{x}$ . Therefore, it does not affect the scaling law for the quality of the ghost image and for the present can be safely taken as a constant. We define  $C_m = \langle I_o^m \rangle$  and  $B_n = \langle I_r^n(\vec{x}) \rangle$ , and we would like to compare the qualities of the ghost images calculated by

$$g_{mn}(\vec{x}) = \frac{1}{C_m B_n} M[I_o^m I_r^n(\vec{x})], \quad (15)$$

and by

$$g'_{mn}(\vec{x}) = \frac{1}{C_m} \frac{M[I_o^m I_r^n(\vec{x})]}{M[I_r^n(\vec{x})]}. \quad (16)$$

It should be noted that  $g_{mn}(\vec{x})$  is equivalent to the unnormalized ghost image  $G_{mn}(\vec{x}) = M[I_o^m I_r^n(\vec{x})]$ . In particular,  $g_{1,1}(\vec{x}) \propto G(\vec{x})$  with  $G(\vec{x}) = G_{1,1}(\vec{x})$  given in Eq. (1). Therefore, according to Ref. [22], there is an optimal contrast-to-noise ratio for the high-order ghost image  $g_{mn}(\vec{x})$  that scales as  $\text{CNR}(g_{\text{opt}}) \propto \sqrt{N/T}$ , with the optimal exponents  $m \sim \sqrt{T}$  and  $n = 1$  or  $2$ .

Before presenting the analysis for  $g'_{mn}(\vec{x})$ , we show the results of numerical simulations using Eqs. (15) and (16). In the simulations, we have taken the illuminating beam to be spatially incoherent, i.e.,  $I(\vec{x}) = |E(\vec{x})|^2$  with  $\langle E^*(\vec{x})E(\vec{x}') \rangle = \mu \delta(\vec{x} - \vec{x}')$ , where the electric field  $E(\vec{x})$  follows circular complex Gaussian statistics. The object mask used is depicted in Fig. 2(a), and the number of transmitting pixels of the object is  $T = 410$ . The number of samplings used is  $N = 150000$ . For the value of  $T$  used in the simulation, the optimal exponents for the correlation  $g_{mn}(\vec{x})$  are  $m \approx 20$  and  $n = 2$ , and  $\text{CNR}(g_{20,2}) \approx 20 \text{CNR}(g_{1,1})$ .

From Figs. 2(c) and 2(d), it is seen that the conventional ghost image  $g_{1,1}(\vec{x})$  is barely visible, while the optimal high-order ghost image  $g_{20,2}(\vec{x})$  has very good quality. It is noted that the averaged speckle pattern  $M[I_r(\vec{x})]$  (Fig. 2(b)) is not uniform. More importantly, it is correlated with the ghost image as can be seen by comparing Figs. 2(b) and 2(c). On the contrary, when Eq. (16) is used to calculate the ghost image, Figs. 2(e) and 2(f) show that the quality of the normalized conventional ghost image is the same as that of the high-order ghost image. It is also noted that while the visibility of the high-order ghost image is much larger than that of the conventional ghost image (see the scale bars in Fig. 2), the signal fluctuations of the high-order ghost image are also larger than that of the conventional ghost image. This is shown explicitly in Fig. 3 in which the probability density functions of the ghost image signals inside and outside the transmitting regions are plotted.

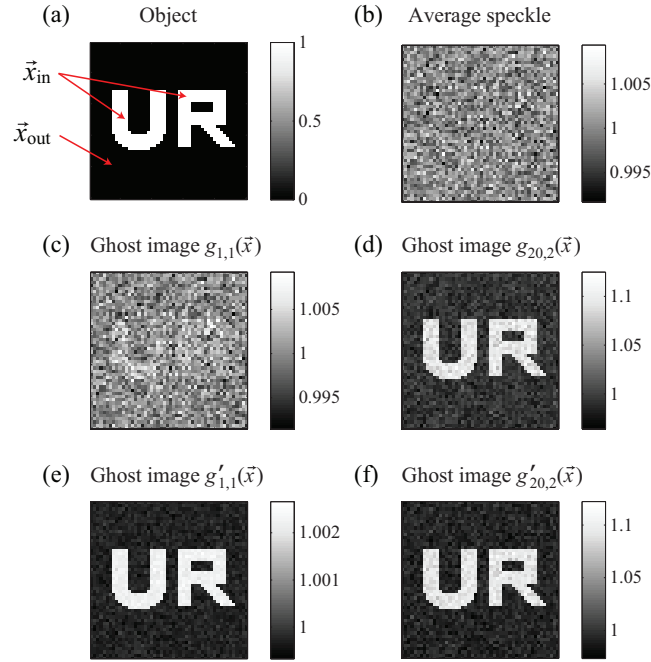


Fig. 2. Numerical simulations. (a) The object mask ( $50 \times 50$  pixels). (b) The averaged speckle pattern  $M[I_r(\vec{x})]$ . (c) The conventional ghost image  $g_{1,1}(\vec{x})$ . (d) The optimal high-order ghost image  $g_{\text{opt}}(\vec{x}) = g_{20,2}(\vec{x})$ . (e) The normalized conventional ghost image  $g'_{1,1}(\vec{x})$ . (f) The normalized high-order ghost image  $g'_{20,2}(\vec{x})$ . The number of transmitting pixels is  $T = 410$  and the number of samplings is  $N = 150000$ . The latter is chosen to be large to make the ghost image in (c) visible.

To understand the properties of  $g'_{mn}(\vec{x})$ , it should be realized that, for large  $N$ ,  $M[I_o^m I_r^n(\vec{x})]$  and  $M[I_r^n(\vec{x})]$  behave as normal random variables with means

$$A_{mn}(\vec{x}) = \langle I_o^m I_r^n(\vec{x}) \rangle, \quad B_n = \langle I_r^n(\vec{x}) \rangle, \quad (17)$$

and variances

$$\alpha_{mn}^2(\vec{x}) = \frac{\Delta^2 [I_o^m I_r^n(\vec{x})]}{N}, \quad \beta_n^2 = \frac{\Delta^2 [I_r^n(\vec{x})]}{N}, \quad (18)$$

by virtue of the central limit theorem. This implies that  $g'_{mn}(\vec{x})$  is a ratio of two normal random variables, and the form of the probability density function of  $g'_{mn}(\vec{x})$  is given in Ref. [30]. It is noted that in general the moments of the ratio of two normal random variables do not exist, especially when the denominator can vanish [31]. However, in our case,  $M[I_r^n(\vec{x})] \neq 0$ . In particular, when  $B_n \gtrsim 3\beta_n$ , it has been shown that the function

$$t_{mn}(\vec{x}) = \frac{B_n C_m g'_{mn}(\vec{x}) - A_{mn}(\vec{x})}{\sqrt{\beta_n^2 C_m^2 g_{mn}'^2(\vec{x}) - 2\rho_{mn}(\vec{x}) C_m g'_{mn}(\vec{x}) + \alpha_{mn}^2(\vec{x})}} \quad (19)$$

is normally distributed with zero mean and unity variance [32], i.e.,

$$P(t_{mn}(\vec{x})) = \frac{1}{\sqrt{2\pi}} \exp\left[-\frac{t_{mn}^2(\vec{x})}{2}\right]. \quad (20)$$

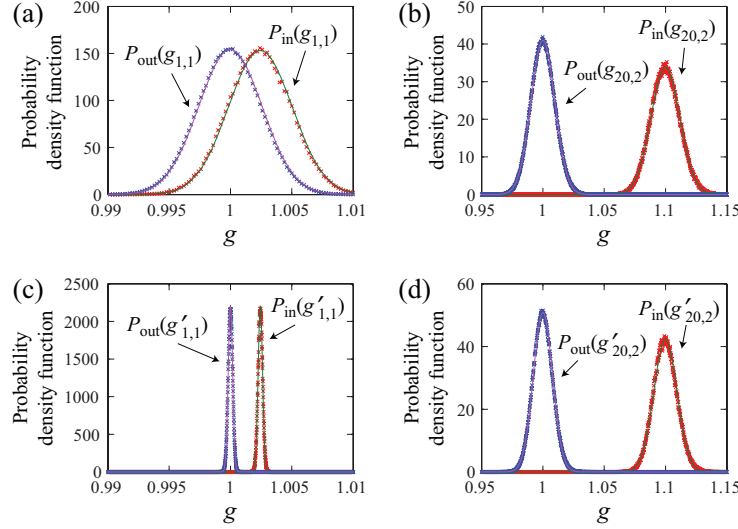


Fig. 3. The probability density functions (pdf) of  $g_{mn}$  and  $g'_{mn}$  inside and outside the transmitting regions of the object with  $P_i(g_{mn}) \equiv P(g_{mn}(\vec{x}_i))$ ,  $i$  = in or out. (a) The pdf for the conventional ghost image  $P_i(g_{1,1})$ . (b) The pdf for the optimal high-order ghost image  $P_i(g_{20,2})$ . (c) The pdf for the normalized conventional ghost image  $P_i(g'_{1,1})$ . (d) The pdf for the normalized high-order ghost image  $P_i(g'_{20,2})$ . The number of transmitting pixels is  $T = 410$  and the number of samplings is  $N = 150000$ . These give  $\langle g_{1,1}(\vec{x}_{in}) \rangle = \langle g'_{1,1}(\vec{x}_{in}) \rangle = 1.0024$  and  $\langle g_{20,2}(\vec{x}_{in}) \rangle = \langle g'_{20,2}(\vec{x}_{in}) \rangle = 1.0998$ . The data points are accumulated by repeating the simulations for 500 times. The solid curves (overlapping with the numerical data) are the theoretical results using Eq. (20).

Here  $\rho_{mn}(\vec{x})$  is the covariance of  $M[I_o^m I_r^n(\vec{x})]$  and  $M[I_r^n(\vec{x})]$ . Moreover, if  $B_n \gg \beta_n$ , the probability density function of  $g'_{mn}(\vec{x})$  tends to be a normal distribution.

Using Eq. (7), we find that

$$A_{mn}(\vec{x}) = \begin{cases} \frac{\Gamma(T+m+n)n!}{\Gamma(T+n)} \mu^{m+n}, & \text{for } \vec{x} = \vec{x}_{in}, \\ \frac{\Gamma(T+m)n!}{\Gamma(T)} \mu^{m+n}, & \text{for } \vec{x} = \vec{x}_{out}, \end{cases} \quad (21)$$

$$B_n = n! \mu^n, \quad C_m = \frac{\Gamma(T+m)}{\Gamma(T)} \mu^m, \quad (22)$$

$$\alpha_{mn}^2(\vec{x}) = \frac{A_{2m} A_{2n}(\vec{x}) - A_{mn}^2(\vec{x})}{N}, \quad \beta_n^2 = \frac{B_{2n} - B_n^2}{N}, \quad (23)$$

and

$$\rho_{mn}(\vec{x}) = \frac{A_{m} A_{2n}(\vec{x}) - A_{mn}(\vec{x}) B_n}{N}. \quad (24)$$

The theoretical probability density functions of the ghost images are plotted in Fig. 3(b) using Eq. (20) and an excellent agreement between the theory and the simulation results is seen.

An approximation to Eq. (20) can be made by putting  $g'_{mn}(\vec{x}) = \langle g'_{mn}(\vec{x}) \rangle$  in the denominator

of  $t_{mn}(\vec{x})$ . The probability density function for  $g'_{mn}(\vec{x})$  is then found to be

$$P(g'_{mn}(\vec{x})) \approx \frac{1}{\sqrt{2\pi}\Delta_{mn}(\vec{x})} \exp\left[-\frac{[g'_{mn}(\vec{x}) - \langle g'_{mn}(\vec{x}) \rangle]^2}{2\Delta_{mn}^2(\vec{x})}\right]. \quad (25)$$

The mean of  $g'_{mn}(\vec{x})$  is given by

$$\langle g'_{mn}(\vec{x}) \rangle = \frac{A_{mn}(\vec{x})}{C_m B_n(\vec{x})} = \begin{cases} \frac{\Gamma(T)\Gamma(T+m+n)}{\Gamma(T+m)\Gamma(T+n)}, & \text{for } \vec{x} = \vec{x}_{\text{in}}, \\ 1, & \text{for } \vec{x} = \vec{x}_{\text{out}}, \end{cases} \quad (26)$$

and the variance of  $g'_{mn}(\vec{x})$  is given by

$$\Delta_{mn}^2(\vec{x}_{\text{in}}) = \frac{(2n)!}{N(n!)^2} \left[ \frac{\Gamma(T+2m+2n)\Gamma(T)^2}{\Gamma(T+m)^2\Gamma(T+2n)} + \frac{\Gamma(T+m+n)^2\Gamma(T)^2}{\Gamma(T+m)^2\Gamma(T+n)^2} - \frac{2\Gamma(T+m+n)\Gamma(T+m+2n)\Gamma(T)^2}{\Gamma(T+m)^2\Gamma(T+n)\Gamma(T+2n)} \right], \quad (27)$$

and

$$\Delta_{mn}^2(\vec{x}_{\text{out}}) = \frac{(2n)!}{N(n!)^2} \left[ \frac{\Gamma(T+2m)\Gamma(T)}{\Gamma(T+m)^2} - 1 \right]. \quad (28)$$

Using these results, we calculate the CNR as

$$\text{CNR}(g'_{mn}) = \frac{\langle g'_{mn}(\vec{x}_{\text{in}}) \rangle - \langle g'_{mn}(\vec{x}_{\text{out}}) \rangle}{\sqrt{\frac{1}{2}[\Delta_{mn}^2(\vec{x}_{\text{in}}) + \Delta_{mn}^2(\vec{x}_{\text{out}})]}}. \quad (29)$$

For example,  $\text{CNR}(g'_{1,1}) = \sqrt{N/(2T+3)}$  and  $\text{CNR}(g'_{1,2}) = \sqrt{N/(3T/2+6)}$ .

When  $T \gg m$  and  $n$ , it can be shown that

$$g'_{mn}(\vec{x}_{\text{in}}) \sim 1 + \frac{mn}{T}, \quad g'_{mn}(\vec{x}_{\text{out}}) = 1, \quad (30)$$

and

$$\Delta_{mn}^2(\vec{x}_{\text{in}}) \approx \Delta_{mn}^2(\vec{x}_{\text{out}}) \sim \frac{m^2(2n)!}{NT(n!)^2}. \quad (31)$$

Then the CNR with  $T \gg m, n$  is found to be

$$\text{CNR}(g'_{mn}) \sim \sqrt{\frac{N}{T}} \left[ \frac{n(n!)}{\sqrt{(2n)!}} \right]. \quad (32)$$

Therefore,  $\text{CNR}(g'_{mn})$  scales as  $\sqrt{N/T}$ , which is the same as the scaling law for  $\text{CNR}(g_{\text{opt}})$  and  $\text{CNR}(G')$ . Figure 4 shows the theoretically predicted  $\text{CNR}(g'_{mn})$  calculated using Eq. (29). Numerical results using  $N = 20000$  are also shown and agree with the analytical results. The deviation of the numerical data from the theory for  $g'_{5,5}$  and  $g'_{20,2}$  is due to the finite number of samplings used in the simulations and is found to improve when a larger  $N$  is used.

From the large  $T$  limit of  $\Delta_{mn}(\vec{x})$ , we see that the noise of the high-order ghost image increases linearly with the object signal order  $m$  and exponentially with the reference signal order  $n$ . Moreover, the CNR is independent of  $m$ . Finally, Eq. (32) demonstrates that the optimal value for  $n$  is 1 or 2.

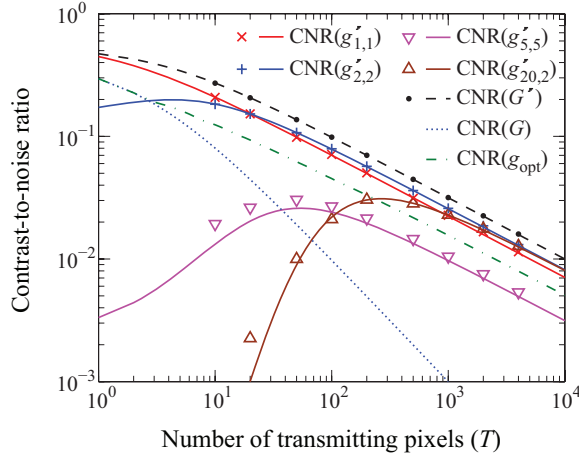


Fig. 4. Plots of the contrast-to-noise ratio  $\text{CNR}(g'_{mn})$  (normalized by  $\sqrt{N}$ ) against the number of transmitting pixels  $T$  for various values of  $m$  and  $n$ . The theoretical curves are plotted using Eq. (29). The data points are from simulations using  $N = 20000$ . Also shown are  $\text{CNR}(G)$  from Eq. (8),  $\text{CNR}(G')$  from Eq. (10) and  $\text{CNR}(g_{\text{opt}})$  from Ref. [22]. We note that under all circumstances the function  $G'$  produces the best image, with procedures  $g'_{1,1}$  and  $g'_{2,2}$  performing nearly as well.

Since the CNR is not quite dependent on  $m$ , one can take a very large value of  $m$  in order to achieve high visibility, which is given by [22]

$$V \equiv \frac{\langle g'_{mn}(\vec{x}_{\text{in}}) \rangle - \langle g'_{mn}(\vec{x}_{\text{out}}) \rangle}{\langle g'_{mn}(\vec{x}_{\text{in}}) \rangle + \langle g'_{mn}(\vec{x}_{\text{out}}) \rangle} \approx \tanh\left(\frac{mn}{2T}\right). \quad (33)$$

The results explain the experimental observations [23] that a large  $m$  and a small  $n$  are preferable in high-order thermal ghost imaging.

#### 4. Effects of shot noise

In Sections 2 and 3, the contrast-to-noise ratios are calculated under the assumption that the light beams are sufficiently intense so that the noise properties of the signals are dominated by the statistics of the speckle fields. Depending on the illumination power on the photodetectors, other noise sources, such as shot noise and dark current, contribute to a certain extent to the signal statistics. The intent of the present section is to study the effect of detection noise on the quality of the ghost image and to determine the conditions under which these additional noise sources are negligible so that the results of Sections 2 and 3 are valid. For definiteness, we assume that shot noise is the only noise source that is present, and that sources of technical noise have been rendered negligibly small.

Based on the assumptions made to the bucket and reference detectors in Section 2, the photocurrents output from the detectors during the reception of an optical pulse of *known* intensity  $I_a$  with  $a = o, r$  are

$$i_a = e \frac{n_{\Delta} I_a}{\mu}, \quad (34)$$

where  $e$  is the electron charge and  $n_{\Delta}$  is the average number of photoelectrons ejected by a detector element, which is defined by

$$n_{\Delta} = \frac{\eta \mu \Delta \tau}{h\nu}, \quad (35)$$

where  $\eta$  is the quantum efficiency of the detector,  $\Delta$  is the area of the pixel,  $\tau$  is the integration time of detection process,  $\nu$  is the frequency of the light, and  $h$  is the Planck constant. We have assumed that the quantum efficiencies of the bucket and reference detectors are the same for convenience.

According to the semiclassical theory of photodetection, the photocurrent is governed by Poisson statistics. The  $n^{\text{th}}$  moment of  $i_a$  is given by

$$\langle i_a^n \rangle_{\text{shot noise}} = e^n \phi_n \left( \frac{n_\Delta}{\mu} I_a \right) \equiv e^n \left( \frac{n_\Delta}{\mu} \right)^n \{I_a\}_n, \quad (36)$$

where  $\phi_n(z)$  are the exponential polynomials [33, 34]. The ensemble averages of the object and reference signals over the intensity of the speckle fields in the calculations of the mean and variance of the ghost image are thus replaced by

$$\begin{aligned} \langle I_o^m I_r^n(\vec{x}) \rangle &\rightarrow \langle \{I_o\}_m \{I_r(\vec{x})\}_n \rangle \\ &= \left( \frac{\mu}{n_\Delta} \right)^{m+n} \left\langle \phi_m \left( \frac{n_\Delta}{\mu} I_o \right) \phi_n \left( \frac{n_\Delta}{\mu} I_r(\vec{x}) \right) \right\rangle, \end{aligned} \quad (37)$$

with  $m, n \geq 0$ . Equation (37) can also be written as

$$\left( \frac{\mu}{n_\Delta} \right)^{m+n} \left\langle \phi_m \left( \frac{n_\Delta}{\mu} I_o \right) \phi_n \left( \frac{n_\Delta}{\mu} I_r(\vec{x}) \right) \right\rangle = \left( \frac{\mu}{n_\Delta} \right)^{m+n} \sum_{i=0}^m \sum_{j=0}^n S(m, i) S(n, j) \frac{\langle i_o^i i_r^j(\vec{x}) \rangle}{\mu^{i+j}} n_\Delta^{i+j}, \quad (38)$$

where  $S(n, k)$  is the Stirling number of the second kind. It is then seen that the high-order correlations of  $I_o$  and  $I_r(\vec{x})$  also involve the contributions from lower order correlations. Note that, for the case of single beam ghost imaging [5], the Poisson shot noise appears only in the bucket detector. In this case, the cross-correlation in the calculation of the ghost image is  $\langle \{I_o\}_m I_r^n(\vec{x}) \rangle$  instead of  $\langle \{I_o\}_m \{I_r(\vec{x})\}_n \rangle$ .

As an illustration, we calculate the CNR with shot noise for the conventional ghost image with background subtraction [cf. Eq. (9)] in the large  $N$  limit. The mean of the ghost image is given by

$$\langle G^{(\text{sn})'}(\vec{x}) \rangle = \left( \frac{\mu}{n_\Delta} \right)^2 \left\langle \phi_1 \left( \frac{n_\Delta}{\mu} I_o - \frac{n_\Delta}{\mu} \langle I_o \rangle \right) \phi_1 \left( \frac{n_\Delta}{\mu} I_r(\vec{x}) - \frac{n_\Delta}{\mu} \langle I_r(\vec{x}) \rangle \right) \right\rangle, \quad (39)$$

and the variance is

$$\begin{aligned} \Delta^2 G^{(\text{sn})'}(\vec{x}) &= \frac{1}{N} \left\{ \left( \frac{\mu}{n_\Delta} \right)^4 \left\langle \phi_2 \left( \frac{n_\Delta}{\mu} I_o - \frac{n_\Delta}{\mu} \langle I_o \rangle \right) \phi_2 \left( \frac{n_\Delta}{\mu} I_r(\vec{x}) - \frac{n_\Delta}{\mu} \langle I_r(\vec{x}) \rangle \right) \right\rangle \right. \\ &\quad \left. - \left[ G^{(\text{sn})'}(\vec{x}) \right]^2 \right\}. \end{aligned} \quad (40)$$

Using  $\phi_1(z) = z$ ,  $\phi_2(z) = z^2 + z$  and Eq. (21), the signal-to-noise ratio is found to be

$$\frac{\langle G^{(\text{sn})'}(\vec{x}) \rangle}{\Delta G^{(\text{sn})'}(\vec{x})} = \sqrt{\frac{NO(\vec{x})}{[T + 7O(\vec{x})] + O(\vec{x})[4n_\Delta^{-1} + n_\Delta^{-2}]}}, \quad (41)$$

where  $O(\vec{x})$  is the binary object function. The corresponding CNR is

$$\text{CNR}(G^{(\text{sn})'}) = \sqrt{\frac{N}{(T + 7/2) + (4n_\Delta^{-1} + n_\Delta^{-2})/2}}. \quad (42)$$

Equation (41) gives the correct dependence on the intensity  $\mu$  when compared to the full quantum approach [28]. The form of  $\text{CNR}(G^{(\text{sn})'})$  is the same as that in Eq. (13) except for an additional second term in the denominator. When  $T \gg 1$  or  $n_\Delta > 10$ , the contribution from shot noise to the CNR becomes insignificant. For high-order thermal ghost imaging, the reference signal order  $n$  is kept to be small. It is checked numerically that the difference between  $\langle \{I_o\}_m \{I_r(\vec{x})\}_n \rangle$  and  $\langle I_o^m I_r^n(\vec{x}) \rangle$  is less than 5% for  $m \leq 50$ ,  $n \leq 4$  and  $T \geq 100$  with  $n_\Delta \geq 200$ .

In our laboratory, we perform pseudo-thermal ghost imaging experiment using a pulsed laser with power  $\sim 100$  mW, pulse duration  $\sim 100$  fs and repetition rate  $\sim 15$  Hz. After scattered by the diffuser (ground glass plate), the energy of the light registered by the bucket detector is measured to be about 1 nJ. The object transmission area is about  $5 \text{ mm}^2$  and the pixel size of the CCD camera (reference detector) is about  $10 \text{ }\mu\text{m}^2$ . Therefore, the energy of light on a CCD pixel is (assuming the CCD has the same quantum efficiency as the bucket detector) about  $1 \text{ nJ}/(5 \text{ mm}^2) \times (10 \text{ }\mu\text{m}^2)$ . The wavelength of the laser is 780 nm. Therefore, the number of photoelectrons per pixel per pulse is

$$n_\Delta = \frac{\eta \mu \Delta \tau}{hc/\lambda} = \frac{10^{-9}/(5 \times 10^{-6}) \times (10 \times 10^{-12})}{(6.63 \times 10^{-34}) \times (3 \times 10^8)/(780 \times 10^{-9})} \sim 7800. \quad (43)$$

With more than a thousand photons per pixel, the shot noise is thus negligible.

## 5. Conclusions

We have analyzed the performances of several common methods of processing the data of thermal ghost imaging. It is found that the contrast-to-noise ratio (CNR) of conventional thermal ghost imaging using simply the averages of the product of the object and reference signal ( $G(\vec{x})$ ) scales as  $\sqrt{N}/T$ , whereas that utilizing the correlation with background subtraction ( $G'(\vec{x})$ ) or background normalization ( $g'_{1,1}(\vec{x})$ ) scales as  $\sqrt{N/T}$ , in which  $N$  is the number of measurements and  $T$  is the number of transmitting pixels of the object. We have also shown analytically that the CNR of the normalized high-order ghost image  $g'_{mn}(\vec{x})$  scales as  $\sqrt{N/T}$ , which is independent of the exponents of the high-order correlation.

We note that, by choosing a large object signal order  $m$  and a small reference signal order  $n$  in the high-order ghost imaging, both the visibility and the contrast-to-noise ratio can be increased substantially at the same time. The results are consistent with the experimental observations reported in Ref. [23]. Finally, a semiclassical photodetection analysis is performed to justify the approach and the applicable regime of the classical method used in the calculations in this paper.

## Acknowledgments

This research is supported by Rochester Optical Manufacturing Company and the US Army Research Office under a Multidisciplinary University Research Initiative (MURI) grant.